

# Thin-film $\text{Sb}_2\text{Se}_3$ photovoltaics with oriented one-dimensional ribbons and benign grain boundaries

Ying Zhou<sup>1,2</sup>, Liang Wang<sup>1,2</sup>, Shiyu Chen<sup>3</sup>, Sikai Qin<sup>1,2</sup>, Xinsheng Liu<sup>1,2</sup>, Jie Chen<sup>1,2</sup>, Ding-Jiang Xue<sup>1,2</sup>, Miao Luo<sup>1,2</sup>, Yuanzhi Cao<sup>1</sup>, Yibing Cheng<sup>1</sup>, Edward H. Sargent<sup>4</sup> and Jiang Tang<sup>1,2\*</sup>

**Solar cells based on inorganic absorbers, such as Si, GaAs, CdTe and  $\text{Cu}(\text{In,Ga})\text{Se}_2$ , permit a high device efficiency and stability. The crystals' three-dimensional structure means that dangling bonds inevitably exist at the grain boundaries (GBs), which significantly degrades the device performance via recombination losses. Thus, the growth of single-crystalline materials or the passivation of defects at the GBs is required to address this problem, which introduces an added processing complexity and cost. Here we report that antimony selenide ( $\text{Sb}_2\text{Se}_3$ )—a simple, non-toxic and low-cost material with an optimal solar bandgap of  $\sim 1.1$  eV—exhibits intrinsically benign GBs because of its one-dimensional crystal structure. Using a simple and fast ( $\sim 1 \mu\text{m min}^{-1}$ ) rapid thermal evaporation process, we oriented crystal growth perpendicular to the substrate, and produced  $\text{Sb}_2\text{Se}_3$  thin-film solar cells with a certified device efficiency of 5.6%. Our results suggest that the family of one-dimensional crystals, including  $\text{Sb}_2\text{Se}_3$ ,  $\text{SbSeI}$  and  $\text{Bi}_2\text{S}_3$ , show promise in photovoltaic applications.**

The urgent need for high-efficiency, low-cost solar cells drives the sustained research on new absorber materials for thin-film photovoltaics. Copper zinc tin sulfide (CZTS) and organic–inorganic metal halide perovskites (for example,  $\text{CH}_3\text{NH}_3\text{PbI}_3$ ) are emerging and promising absorber materials that have achieved impressive certified device efficiencies<sup>1,2</sup>. However, the complexity of defect physics associated with CZTS<sup>3,4</sup> appears to limit further significant efficiency improvements in this system, and concerns over stability and the reliance on lead in  $\text{CH}_3\text{NH}_3\text{PbI}_3$  (ref. 5) creates the need for new, stable, Pb-free materials.

These and other widely explored photovoltaic absorber materials (such as Si, GaAs, CdTe, InP and  $\text{Cu}(\text{In,Ga})\text{Se}_2$  (CIGS)) exhibit a three-dimensional (3D) crystal structure<sup>6–8</sup>, that is, they are bound by covalent and/or ionic bonds in all three spatial dimensions. The 3D crystal structure guarantees an isotropic carrier transport and permits a relaxed orientation control. However, at discontinuities such as GBs, dangling bonds typically act as recombination centres, and require further steps to be remedied<sup>9–11</sup>. For example, in CdTe (Fig. 1a) recombination loss through dangling bonds at the GBs lowers the open-circuit voltage ( $V_{\text{OC}}$ ) even when the best-available passivation methods are employed<sup>12</sup>.

We hypothesized that materials possessing a one-dimensional (1D) crystal structure (Fig. 1b), such as the ribboned compounds  $\text{Sb}_2\text{Se}_3$  and  $\text{Bi}_2\text{S}_3$ , could, if suitably oriented, offer a compelling performance. In  $\text{Sb}_2\text{Se}_3$ , for example,  $(\text{Sb}_4\text{Se}_6)_n$  ribbons stack along the [001] direction through strong covalent Sb–Se bonds, whereas in the [100] and [010] directions the  $(\text{Sb}_4\text{Se}_6)_n$  ribbons are held together by van der Waals forces. Rarely have these materials been explored for photovoltaics because of concerns about the poor carrier transport between the ribbons, and worries about the mechanical stability of the films.

We posited that a new materials-processing strategy designed to orient ribbons vertically on the substrate could permit photogenerated carriers to travel efficiently along the covalently bonded 1D axis. In the orthogonal direction, the parallel-stacked ribbons would substantially provide no dangling bonds, even at GBs, and thereby minimize recombination losses, which is an important advantage in photovoltaic applications because recombination losses at GBs are one of the major limiting factors for high-efficiency thin-film solar cells.

We began with first-principles simulations (VASP code) to study the structural relaxation and electronic structure of  $\text{Sb}_2\text{Se}_3$  surfaces. The available terminations of (100) and (010) surfaces in  $\text{Sb}_2\text{Se}_3$  require no breaking of the Sb–Se bonds (Fig. 1c) and thus produce **no dangling bonds**. Other surfaces parallel to the [001] direction also have no dangling bonds, for example, the (110) and (120) surfaces. Their surface energy is therefore lower than those of surfaces with dangling bonds, such as the (001), **(211) and (221) surfaces**. Calculation reveals that, as expected, the surface energies for the (100), (010), (110), (120), (001), (211) and (221) surfaces, respectively, are 0.44, 0.25, 0.33, 0.32, 0.46, 0.56 and  $0.53 \text{ J m}^{-2}$ . This indicates that the most-abundant surfaces in  $\text{Sb}_2\text{Se}_3$  samples will be the (010), (110) and (120) surfaces, that is, those with the lowest formation energies and no breakage of the covalent bonds. Density functional theory confirms quantitatively that no extra states are introduced inside the bandgap by these terminations. A clean bandgap is seen in the calculated density of states (DOS) of the four  $\text{Sb}_2\text{Se}_3$  surfaces (Fig. 1d) and the gap is comparable to that of bulk  $\text{Sb}_2\text{Se}_3$ . Furthermore, there is no appreciable change in the calculated DOS over a wide energy range ( $-10$  to  $3 \text{ eV}$ ), which indicates that there is **no significant reconstruction on these surfaces**. In

<sup>1</sup>Wuhan National Laboratory for Optoelectronics (WNLO), Huazhong University of Science and Technology (HUST), Wuhan 430074, China. <sup>2</sup>School of Optical and Electronic Information, Huazhong University of Science and Technology (HUST), Wuhan 430074, China. <sup>3</sup>Key Laboratory for Polar Materials and Devices (MOE), East China Normal University, Shanghai 200241, China. <sup>4</sup>Department of Electrical and Computer Engineering, University of Toronto, Toronto, Ontario M5S 3G4, Canada. \*e-mail: jtang@mail.hust.edu.cn

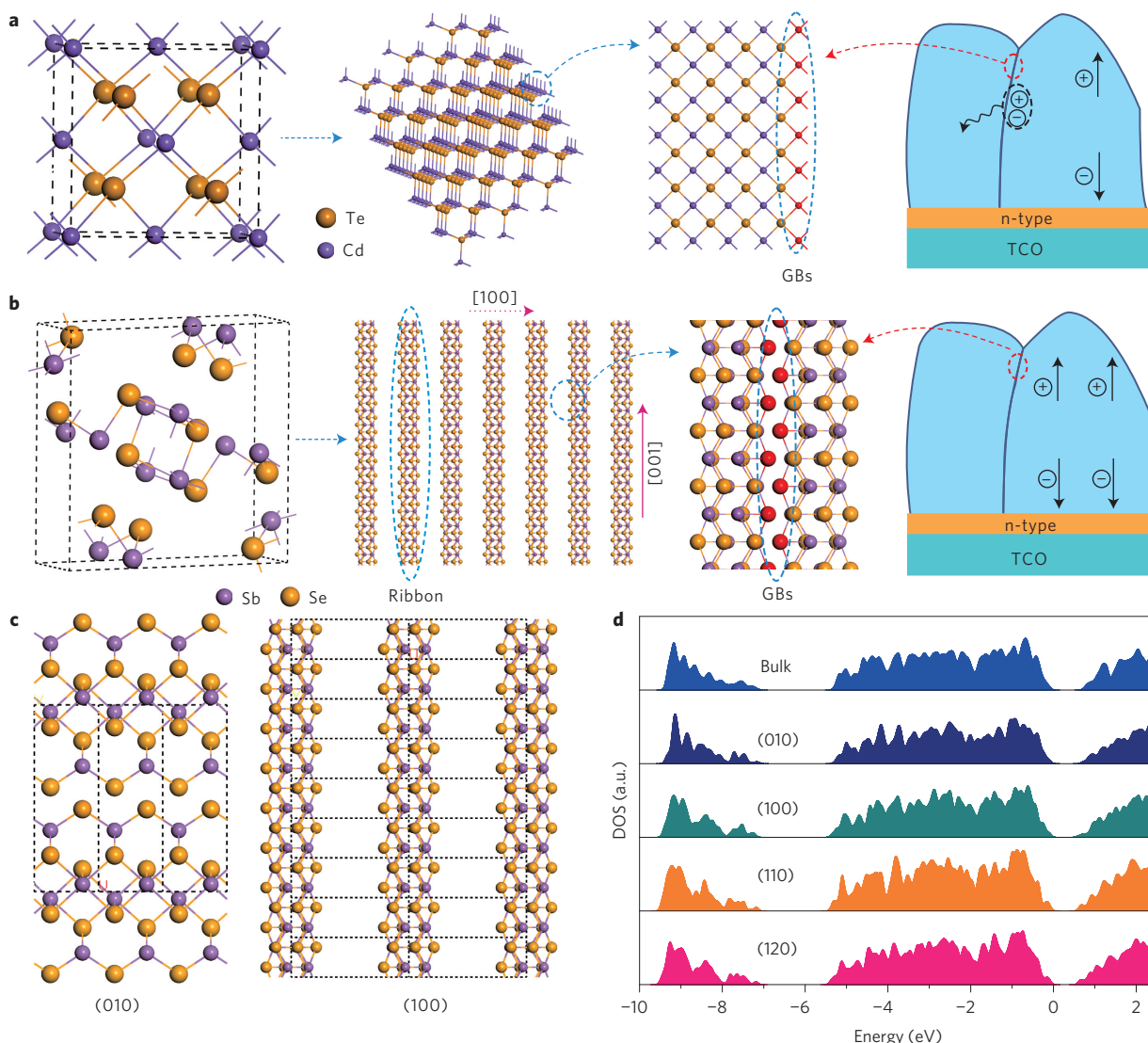


**Figure 1 | Crystal structure, DOS and recombination loss at the GBs in CdTe and Sb<sub>2</sub>Se<sub>3</sub> solar cells.** **a**, CdTe possesses a 3D crystal structure and has dangling bonds (shown as red rods) at the GBs, which act as defects that cause a recombination loss of the photogenerated carriers. **b**, Sb<sub>2</sub>Se<sub>3</sub> (orthorhombic) is composed of (Sb<sub>4</sub>Se<sub>6</sub>)<sub>n</sub> ribbons stacked in parallel in the [001] direction. All the atoms at the edge of these ribbons are saturated (highlighted as red spheres) and introduce no recombination loss at the GBs once they are oriented vertically onto the substrates. For clarity, we omitted from the image those (Sb<sub>4</sub>Se<sub>6</sub>)<sub>n</sub> ribbons that are present underneath this layer, but in a staggered manner. **c**, Atomic configuration of the (010) and (100) surfaces (marked by the dashed black grids) in the Sb<sub>2</sub>Se<sub>3</sub> crystal. **d**, DOS of the bulk Sb<sub>2</sub>Se<sub>3</sub> and of four surfaces that are parallel to the [001] direction. The forbidden gap is the empty zone near 0 eV. TCO, transparent conducting oxide.

sum, the ribbons represent the fundamental building block of the Sb<sub>2</sub>Se<sub>3</sub> structure, and surface reconstruction is negligible as long as this basic repeat unit is not broken.

Overall, this computational study confirms that, as long as the Sb<sub>2</sub>Se<sub>3</sub> ribbons are suitably oriented, the GBs will be terminated by the intrinsically benign surfaces (for example, (100), (010), (110) and (120) planes) and so the recombination loss minimized. This is in striking contrast with most known photovoltaic absorbers, in which the breakage of covalent bonds introduces defect states and recombination centres at the GBs<sup>13–15</sup>.

A number of additional properties make Sb<sub>2</sub>Se<sub>3</sub> particularly worthy of experimental investigation as high-efficiency, low-cost thin-film solar cells<sup>16</sup>. Like CdTe, but in contrast with CIGS and CZTS, Sb<sub>2</sub>Se<sub>3</sub> is a simple binary compound with a fixed phase and stoichiometry. It has a very strong absorption coefficient (>10<sup>5</sup> cm<sup>-1</sup> at short wavelengths) and its bandgap is ~1.1 eV (refs 17,18), optimal for single-junction solar cells. The constituents of

Sb<sub>2</sub>Se<sub>3</sub> are non-toxic and low in cost (Sb has a similar cost to Cu), and, as we proceed to show herein, Sb<sub>2</sub>Se<sub>3</sub> films are produced using minimal energy, which, in principle, enables a short energy-payback time for a solar cell<sup>19</sup>. All of these considerations motivated the further study of oriented Sb<sub>2</sub>Se<sub>3</sub> films and the devices herein.

Sb<sub>2</sub>Se<sub>3</sub> has a low melting point of 608 °C and a high saturated vapour pressure (~1,200 Pa at 550 °C)<sup>20</sup>, which enables us to carry out film deposition using rapid thermal evaporation (RTE) in a tube furnace with a high ramp rate (Supplementary Fig. 1). Sb<sub>2</sub>Se<sub>3</sub> powder was directly applied via evaporation under a low vacuum pressure (~8 mtorr) maintained by a mechanical pump. Once heated, Sb<sub>2</sub>Se<sub>3</sub> powder evaporated and, because of the temperature gradient, condensed on the substrate to form the Sb<sub>2</sub>Se<sub>3</sub> film. The distance between the evaporating source and the substrate was kept at the low value of 0.8 cm to enable a high material usage and fast deposition rate. The deposition rate was as high as 1 μm min<sup>-1</sup>, much greater than that of regular thermal evaporation (typically

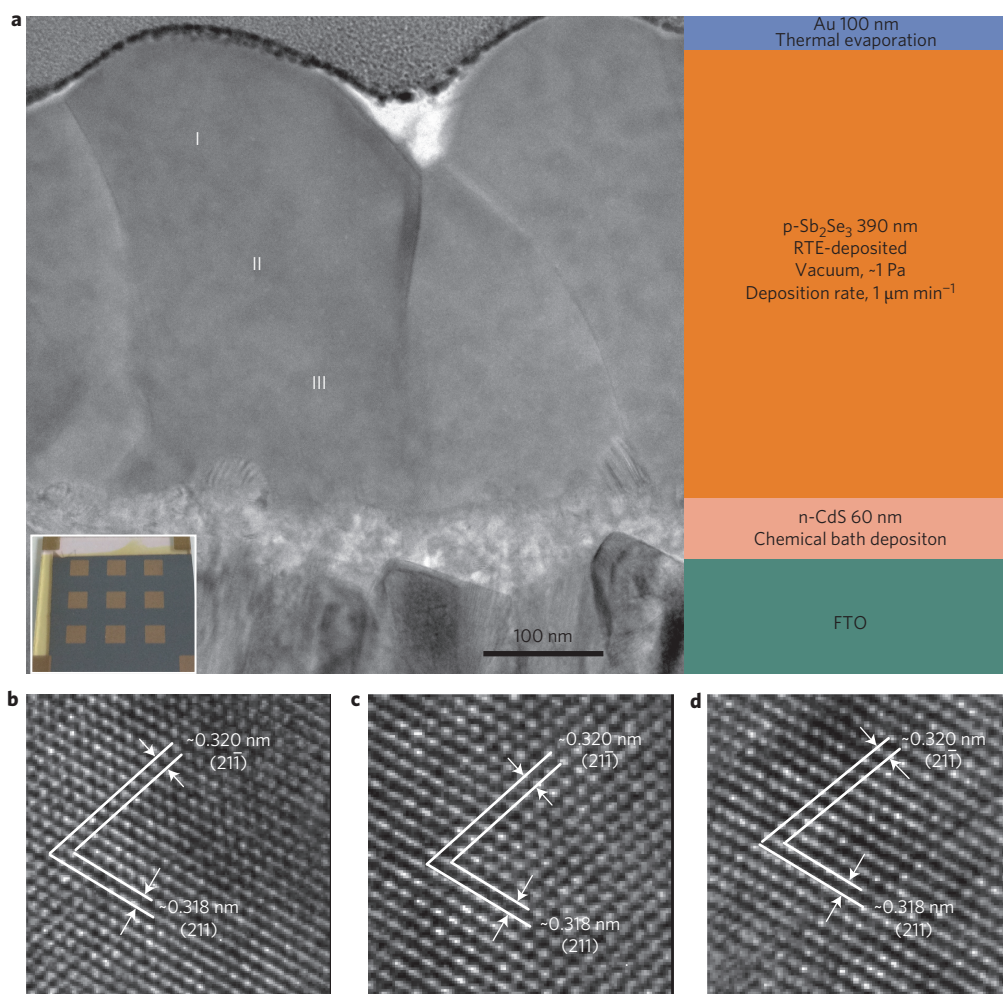


**Figure 2 | Structure and TEM analysis of  $\text{Sb}_2\text{Se}_3$  films and devices.** **a**, Cross-sectional TEM image of the certified device. The nature of each layer and the corresponding preparation procedures are given in the right column. The inset also shows the picture of a finished device; the nine yellow squares are the gold electrodes. HRTEM scans were performed at points I, II and III, and the corresponding lattice fringes are shown in **b–d**.

0.01–0.1  $\mu\text{m min}^{-1}$ ) or sputtering (typically 0.01–0.05  $\mu\text{m min}^{-1}$ ) and comparable to confined-space sublimation (CSS)<sup>21</sup>, a key technology that has enabled the high manufacturing throughput and commercial success of CdTe solar cells. The RTE process is distinct from CSS because, in the RTE performed herein,  $\text{Sb}_2\text{Se}_3$  melts and evaporates from the liquid phase, in contrast to a direct sublimation from the solid. Using this simple and fast technology, phase-pure  $\text{Sb}_2\text{Se}_3$  film (Supplementary Fig. 2) and solar cells were readily fabricated with high reproducibility.

We first analysed, using transmission electron microscopy (TEM), specific regions of the  $\text{Sb}_2\text{Se}_3$  films made in actual solar devices. The full device stack consisted of a fluorine-doped tin oxide (FTO) substrate, a thin (~60 nm) CdS layer produced through chemical bath deposition, an approximately 390 nm thick  $\text{Sb}_2\text{Se}_3$  absorber layer deposited by the RTE process and top Au electrodes from thermal evaporation. For TEM characterization, the sample was prepared by cross-sectioning from the certified device using a focused ion beam. The cross-sectional TEM image showed that the  $\text{Sb}_2\text{Se}_3$  film was compact and composed of large  $\text{Sb}_2\text{Se}_3$  grains of size equal to the film thickness (Fig. 2a). To check whether the grains were single crystalline, we applied high-resolution transmission electron microscopy (HRTEM) to analyse three arbitrarily selected points (I, II and III in Fig. 2a) with the corresponding lattice fringes shown in Fig. 2b–d. The distances between lattice lines were measured as 0.320 nm and 0.318 nm,

which corresponds to the separation of the (21̄1̄) and (211) planes in orthorhombic  $\text{Sb}_2\text{Se}_3$ . The crystal planes extend continuously from the top to the bottom of the active region of the device, which confirms that this grain was single crystalline. This trend was confirmed with further studies of multiple grains (Supplementary Fig. 3), reinforcing the picture that the  $\text{Sb}_2\text{Se}_3$  films are made up of single-crystalline grains.

Orientational control of the  $\text{Sb}_2\text{Se}_3$  film is predicted to be crucial to realize an efficient carrier transport and benign GBs. We investigated, therefore, the possibility of a correlation between  $\text{Sb}_2\text{Se}_3$  film orientation and photovoltaic device performance. Different substrate temperatures ( $T_{\text{sub}}$ ) during the RTE process were explored with an identical  $\text{Sb}_2\text{Se}_3$  film thickness maintained. Devices of Class A were deposited onto the substrate kept at 300 °C, and devices of Class B were deposited onto a 350 °C substrate. Both devices had an area of 0.095  $\text{cm}^2$  defined by the gold electrodes. Typical device performance (Fig. 3a) measured under 100  $\text{mW cm}^{-2}$  illumination (Class 3A solar simulator) revealed a short-circuit current density ( $J_{\text{SC}}$ ) for device Class A of 27.2  $\text{mA cm}^{-2}$ , fill factor (FF) of 53% and series resistance ( $R_{\text{s}}$ ) of 40  $\Omega$ , whereas the corresponding values in device Class B were 18.4  $\text{mA cm}^{-2}$ , 47% and 89  $\Omega$ . We first applied energy-dispersive X-ray spectroscopy (Supplementary Fig. 4 and Supplementary Tables 1–3) and capacitance voltage measurement (Supplementary Fig. 5) to analyse our devices and found out that both the  $\text{Sb}_2\text{Se}_3$  films deposited at substrate temperatures of 300 °C and 350 °C were



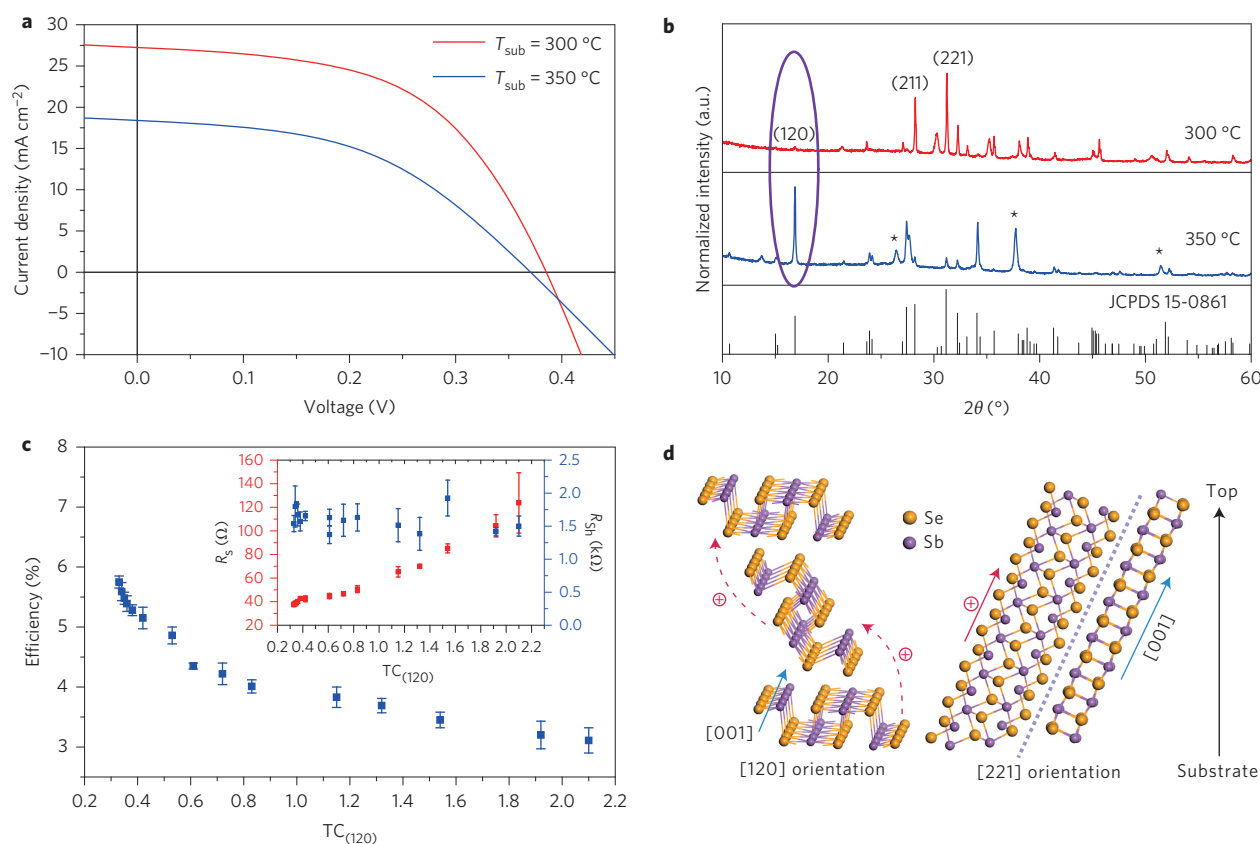


**Figure 3 | Device performance and its correlation with crystalline orientation.** **a, b**, Solar cells with different photovoltaic performance (**a**) and the corresponding XRD patterns (**b**). The standard diffraction pattern for  $Sb_2Se_3$  (JCPDS 15-0861) is included for reference. The asterisks mark the peaks indexed to the FTO substrate. The peak at  $13^\circ$  is associated by indexing to the excess of the trace element Se. **c**, Statistics of the  $TC_{(120)}$  peaks with the device efficiency,  $R_s$  (left axis in the inset) and  $R_{sh}$  (right axis in the inset) of the corresponding devices. To obtain the statistics presented, 140 devices were included. **d**, Atomic structures of [120]- and [221]-oriented grains in  $Sb_2Se_3$ . The substrate is the CdS buffer layer on which the  $Sb_2Se_3$  ribbons grow. On photoexcitation, charge carriers must hop between ribbons in the [120]-oriented grain (dashed red arrows), but are able to move along the [221]-oriented grain smoothly (solid red arrows).

slightly Se rich (the molar ratio Se:Sb was 1.51) and showed a very similar doping density. This indicates that the film composition and consequent doping density probably did not account for the observed device-efficiency difference. The large improvement from device Class B (3.2% efficiency) to Class A (5.6% efficiency) cannot be accounted for by stoichiometry and/or compositional differences, and we instead ascribed it to different film orientations. Indeed, for device Class A, the diffraction intensity associated with the (120) peak was much weaker than that for the (211) peak, whereas in device Class B the intensities of these two peaks were comparable with each other (Fig. 3b).

To quantitate the orientation effects, we calculated the texture coefficient of the (120) ( $TC_{(120)}$ ) peaks from 140 devices and plotted the corresponding device efficiency versus texture coefficient (TC) in Fig. 3c. The TC measures film orientation (Supplementary Fig. 6), with large TCs for a diffraction peak indicating a preferred orientation along this direction<sup>22</sup>. There existed a strong correlation between device performance and film orientation: device efficiency monotonically decreased when the  $TC_{(120)}$  orientation increased. Further analysis revealed that for all of these devices, the shunt resistance ( $R_{sh}$ ) remained constant at approximately 1,600 Ω, which confirms a similar junction quality, whereas  $R_s$  increased monotonically with an increased value of the  $TC_{(120)}$ . We can explain this observation (that the preferred orientation along the [120] direction resulted in a significantly increased  $R_s$  and decreased device efficiency) by the fact that the [120]-oriented grain consists of  $(Sb_4Se_6)_n$  ribbons horizontally stacked in parallel with the substrate

(Fig. 3d). In contrast, a [221]-oriented grain consists of tilted  $(Sb_4Se_6)_n$  ribbons stacked vertically on the substrate. A [211]-oriented grain is also composed of tilted  $(Sb_4Se_6)_n$  ribbons, but to a different angle, and thus we limit our transport discussion to the [221]-oriented grains. Naturally, carrier transport in the [211]-oriented grains should be much easier than in the [120]-oriented grains because in the former carriers travel within the covalently bonded  $(Sb_4Se_6)_n$  ribbons and in the latter carriers are required to hop between ribbons held together by van der Waals forces. Furthermore, GBs of the [211]-oriented grains are composed of planes of low surface energy ( $hk0$ ), such as the (100), (010), (110), (120) planes, which are free of dangling bonds and should cause little recombination loss. In sum, we explain the lower  $R_s$ , better FF and higher  $J_{sc}$  as the result of the improved transport and lowered recombination loss observed in devices with a preferred [211] orientation of the  $Sb_2Se_3$  active layers.

For polycrystalline thin-film solar cells, the passivation of GBs to suppress strong carrier recombination is mandatory to achieve high-efficiency devices. Typical examples are the carefully engineered Cu-deficient GBs in CIGS solar cells<sup>23,24</sup> and a high-temperature  $CdCl_2$  treatment for CdTe solar cells<sup>24,25</sup>. We studied the properties of GBs in our  $Sb_2Se_3$  solar cells using Kelvin probe force microscope (KPFM) and electron-beam-induced current (EBIC) measurements. Two-dimensional topography spatial maps and the corresponding surface potentials of  $Sb_2Se_3$  thin films (Fig. 4a,b) reveal that there is no correlation between GBs (identifiable by notable changes in surface topography) and the substantial potential

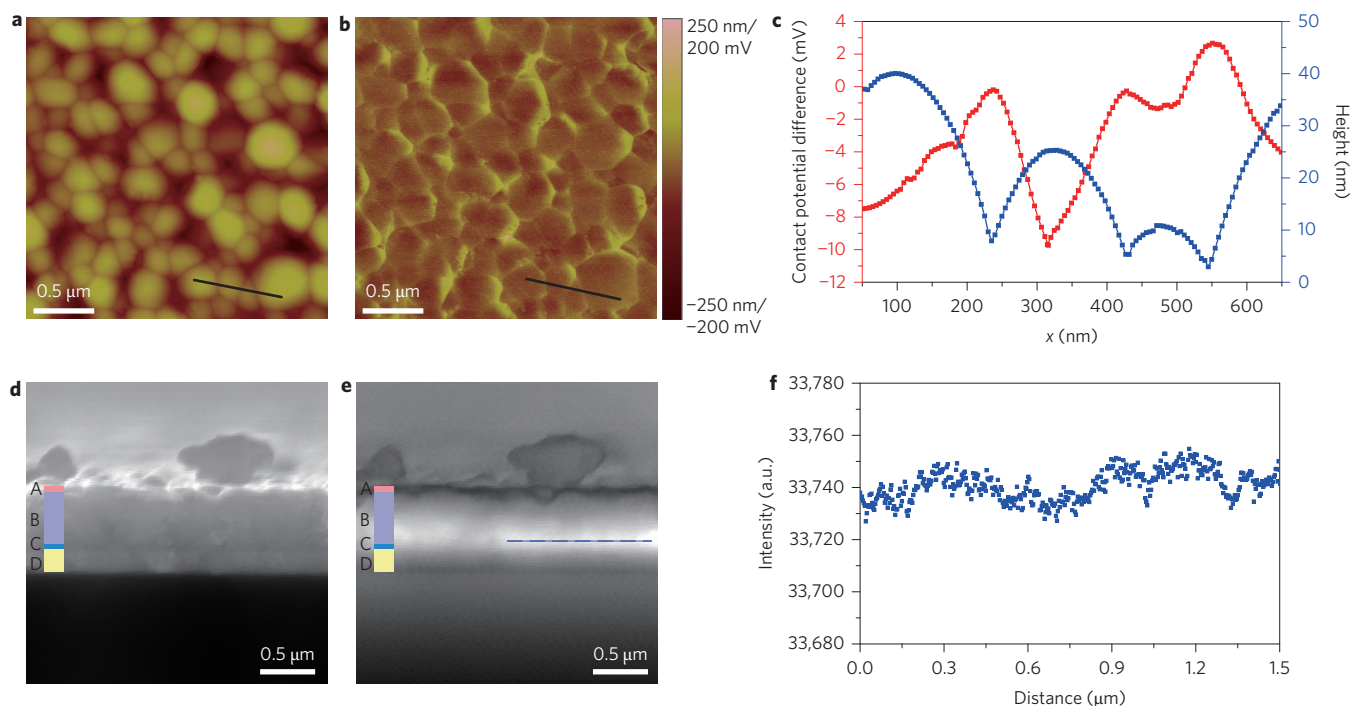


**Figure 4 | Surface potential at  $\text{Sb}_2\text{Se}_3$  GBs and EBIC images from a crystallographically well-oriented device (deposited onto 300 °C substrates).**

**a,b**, Atomic force microscopy (**a**) and scanning KPFM image (**b**) of the device. The scanning area is  $2.5\ \mu\text{m} \times 2.5\ \mu\text{m}$ . **c**, Contact potential difference (red) and height (blue) along the solid black lines drawn in **a** and **b**. The valleys of the height curve correspond to the GBs. **d,e**, Cross-sectional SEM (**d**) and EBIC images (**e**) for the cleaved  $\text{Sb}_2\text{Se}_3$  devices. For the coloured legend, A is Au, B is  $\text{Sb}_2\text{Se}_3$ , C is CdS and D is FTO. White parts indicate the zones in which carriers induced by the electron beam were efficiently collected and grey areas indicate the  $\text{Sb}_2\text{Se}_3$  zones that contributed less photocurrent. **f**, The intensity profiling along the dashed blue line marked in **e**. The scattering in signal intensity is negligible in the scanned  $1.5\ \mu\text{m}$  length, which suggests a uniform photocurrent-collecting efficiency even across GBs.

variation in the KPFM image. Overall, the average roughness of an  $\text{Sb}_2\text{Se}_3$  film is 23 nm and the average surface potential difference is a very low 9.1 mV (much below the thermal energy,  $k_B T$ ). The surface-potential fluctuations are extremely small compared to those of CIGS and CZTS films (generally  $>100\ \text{mV}$  in a  $2.5\ \mu\text{m} \times 2.5\ \mu\text{m}$  zone<sup>9,25</sup>). In an illustrative line scan crossing the GBs (Fig. 4c), the surface potential difference between two grains is as low as 10 mV, which indicates a lack of significant band bending and surface defects in the  $\text{Sb}_2\text{Se}_3$  films.

Further scanning electron microscopy (SEM) and EBIC analyses of the  $\text{Sb}_2\text{Se}_3$  solar cells are reported in Fig. 4d,e, respectively. The thicknesses of the  $\text{Sb}_2\text{Se}_3$  and CdS layers were 390 nm and 60 nm, respectively, which is consistent with the results obtained from the TEM characterization (Fig. 2a). Bright areas in an EBIC image indicate regions of high collection efficiency for minority carriers. Whereas in CdTe and CIGS a high contrast indicates a non-uniform collection efficiency<sup>26</sup>, the  $\text{Sb}_2\text{Se}_3$  solar cell exhibits no appreciable variation in the EBIC signal across the absorber layer close to the CdS layer (Fig. 4e) and, more importantly, also across a  $2\ \mu\text{m}$  long line scan (Fig. 4f). As we have already shown, the same materials processing led to  $\sim 300\ \text{nm}$  grain sizes, results that indicate the EBIC signal, and hence collection efficiency, is uniform over multiple grains, excluding severe carrier recombination or an efficient current-collecting path presented at GBs. The EBIC findings echo the KPFM results above and clearly demonstrate that the GBs and grain interior are indistinguishable in our  $\text{Sb}_2\text{Se}_3$  film, an expected consequence of GBs free of dangling bonds.

We obtained certification of the solar cells reported herein (Fig. 5a,b, Newport Certificate Number (NCN) 1017). In all the devices reported herein, illumination is from the FTO side and photogenerated carriers separate at the p- $\text{Sb}_2\text{Se}_3$ /n-CdS interface. Electrons are injected into the CdS and collected by the FTO, and

holes travel through the  $\text{Sb}_2\text{Se}_3$  absorber and are collected by the back Au ohmic contact. The certified device ( $0.095\ \text{cm}^2$ ) exhibited a  $J_{\text{sc}}$  of  $25.1\ \text{mA cm}^{-2}$ , a  $V_{\text{oc}}$  of 0.40 V and an FF of 55.7%, which corresponds to a power-conversion efficiency (PCE) of 5.6% (Fig. 5a). This agrees with the in-house measurements, and in each case no hysteresis between the forward and reverse scans was observed (Supplementary Fig. 7). We also built large-area ( $1.08\ \text{cm}^2$ ) devices and obtained a device efficiency of 5.4% measured with the aid of aperture and mechanical scribing (Supplementary Figs 8 and 9). This device efficiency surpasses that of many other emerging inorganic solar cells based on Cd-free active absorbers, such as SnS (ref. 27) and  $\text{FeS}_2$  (ref. 28). Measurement of the external quantum efficiency (EQE) showed that the photocurrent contribution extended to 1,070 nm, consistent with the measured optical band gap. By dividing the EQE spectrum by the optical absorption, we obtained an internal quantum efficiency (IQE) close to 100% in the 550–600 nm solar spectrum. The high IQE is again consistent with the low recombination loss assigned to the benign GBs studied in detail herein. The photovoltaic performance obtained across a study of 100 devices (Fig. 5c) demonstrates a tight distribution with an average efficiency of 5.24% and a standard deviation of 0.34%. The device efficiency (Fig. 5d) increased by about 0.3 power points (from 5.32% to 5.66%) when stored in ambient air for up to 45 days without encapsulation, in good agreement with our previous reports of thermally evaporated  $\text{Sb}_2\text{Se}_3$  solar cells<sup>19,29</sup>. Damp-heat testing (85 °C and 85% humidity, no encapsulation) of the same device showed a slightly reduced device performance, from an initial 5.67% efficiency to 5.39% after 10 hours of testing and to 5.16% after 100 hours of testing. This amount of degradation is considerably lower than that of many next-generation solar cells, such as organic–inorganic halide perovskite and polymer solar cells<sup>5</sup>.

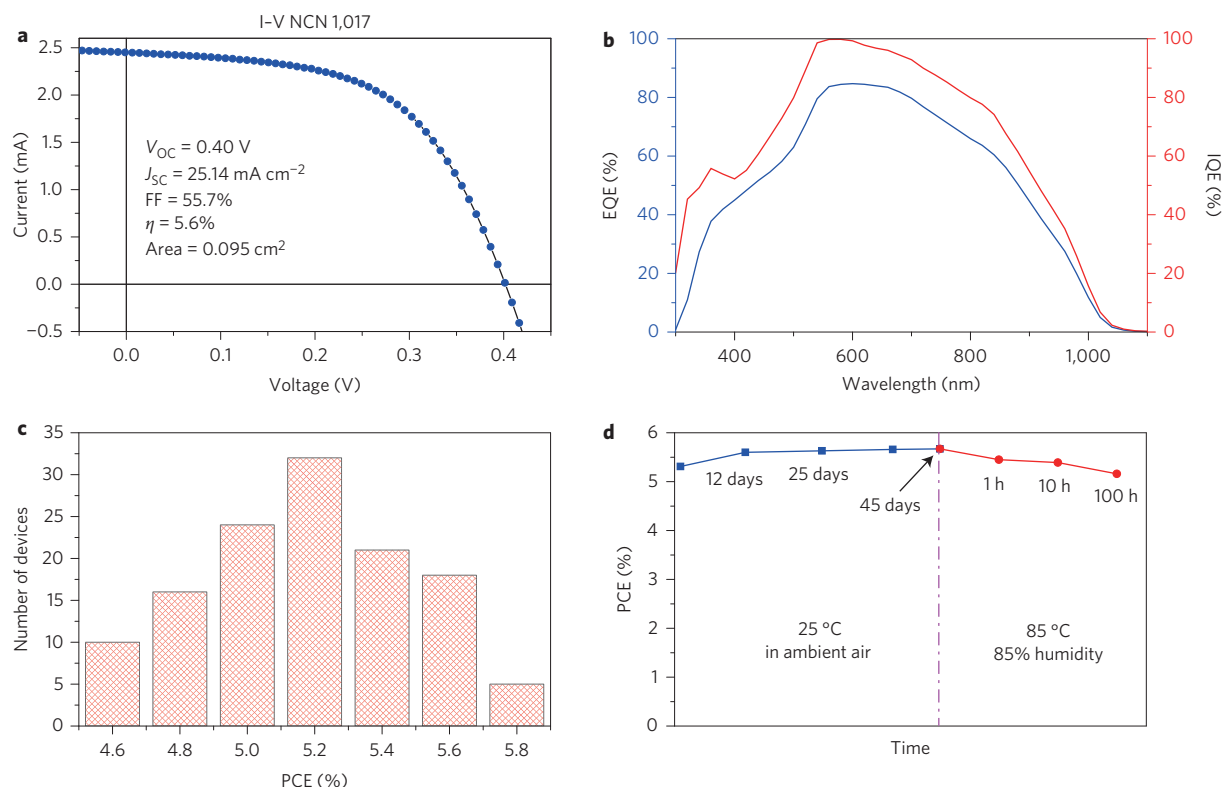


**Figure 5 | Device performance (certified) and stability.** **a,b**, Current–voltage (*I*–*V*) (**a**) and EQE and IQE spectra (**b**) of the FTO/CdS/Sb<sub>2</sub>Se<sub>3</sub>/Au solar cell independently certified by the Newport Cooperation (Calibration Certificate No. 1017). **c**, Histogram of device efficiencies obtained from over 100 individually fabricated devices:  $V_{OC} = 0.385 \pm 0.012$  V,  $J_{SC} = 25.47 \pm 1.75$  mA cm<sup>-2</sup> and FF =  $53.37 \pm 3.72\%$ , with efficiencies of  $5.24 \pm 0.34\%$ . **d**, The stability of a typical device without package stored under regular laboratory conditions (ambient air, no shading) and then subjected to a damp-heat measurement (85 °C, 85% humidity, in the dark).

The path to improved solar PCEs requires major progress on the current (from 25 mA cm<sup>-2</sup> towards the maximum available 42 mA cm<sup>-2</sup> for the 1.1 eV bandgap), the voltage (from 0.4 to 0.75 V for this bandgap) and the FF (from a 50% range into an 80% range). The low EQE at short wavelengths (Fig. 5b) suggests that the CdS front layer should be replaced by a more desirable junction-forming material with a larger bandgap and an environmentally friendly composition, such as TiO<sub>2</sub> or ZnO. Although the ambipolar transport is achieved efficiently over ~150 nm (>80% EQE at a wavelength of 600 nm at which the absorption length is ~150 nm), these materials and devices require an in-depth study to determine whether the minority carrier diffusion length requires extending, or whether an electron-blocking back contact (back surface field) is the major requirement for an improved current. The modest  $V_{OC}$  and FF combined with the evidence of benign GBs suggests that electrical interfaces to Sb<sub>2</sub>Se<sub>3</sub> (for an efficient charge extraction, maximal quasi-Fermi-level splitting and the blocking of one carrier at each interface) deserves significant attention.

In sum, this work presents a non-toxic, stable and manufacturable method of solar-cell fabrication that, in the initial trials, led to a certified device efficiency of 5.6%. The work reveals that materials with a 1D crystal structure, little explored in photovoltaics, offer promise as absorbers once the films are oriented suitably for transport. We have shown that these materials can simultaneously sustain excellent transport along one axis and minimal recombination (owing to the benign GBs) along the orthogonal axes. The family of 1D materials includes other V<sub>2</sub>–VI<sub>3</sub> compounds, such as Bi<sub>2</sub>S<sub>3</sub>, and V–VI–VII compounds, such as SbSeI, which all possess attractive material and optoelectronic properties. Analogously, 2D binary layered materials, such as MoSe<sub>2</sub> and

WSe<sub>2</sub>, when similarly aligned to a substrate are expected to exhibit sufficient transport and manifest the benefits of covalently bonded planes and partially benign GBs.

## Methods

Methods and any associated references are available in the [online version of the paper](#).

Received 11 November 2014; accepted 14 April 2015;  
published online 18 May 2015

## References

- Wang, W. *et al.* Device characteristics of CZTSSe thin-film solar cells with 12.6% efficiency. *Adv. Energy Mater.* **4**, 1301465 (2014).
- Jeon, N. J. *et al.* Solvent engineering for high-performance inorganic–organic hybrid perovskite solar cells. *Nature Mater.* **13**, 897–903 (2014).
- Chen, S., Walsh, A., Gong, X. G. & Wei, S. H. Classification of lattice defects in the kesterite Cu<sub>2</sub>ZnSnS<sub>4</sub> and Cu<sub>2</sub>ZnSnSe<sub>4</sub> earth-abundant solar cell absorbers. *Adv. Mater.* **25**, 1522–1539 (2013).
- Barkhouse, D. A. R., Gunawan, O., Gokmen, T., Todorov, T. K. & Mitzi, D. B. Device characteristics of a 10.1% hydrazine-processed Cu<sub>2</sub>ZnSn(S<sub>2</sub>Se)<sub>4</sub> solar cell. *Prog. Photovolt.* **20**, 6–11 (2012).
- Gratzel, M. The light and shade of perovskite solar cells. *Nature Mater.* **13**, 838–842 (2014).
- Kranz, L. *et al.* Doping of polycrystalline CdTe for high-efficiency solar cells on flexible metal foil. *Nature Commun.* **4**, 2306 (2013).
- Panthani, M. G. *et al.* Synthesis of CuInS<sub>2</sub>, CuInSe<sub>2</sub>, and Cu(In<sub>x</sub>Ga<sub>1-x</sub>)Se<sub>2</sub> (CIGS) nanocrystal ‘links’ for printable photovoltaics. *J. Am. Chem. Soc.* **130**, 16770–16777 (2008).
- Chirilă, A. *et al.* Potassium-induced surface modification of Cu(In,Ga)Se<sub>2</sub> thin films for high-efficiency solar cells. *Nature Mater.* **12**, 1107–1111 (2013).
- Baier, R., Leendertz, C., Abou-Ras, D., Lux-Steiner, M. C. & Sadewasser, S. Properties of electronic potential barriers at grain boundaries in Cu(In,Ga)Se<sub>2</sub> thin films. *Sol. Energ. Mat. Sol. C* **130**, 124–131 (2014).
- Choi, Y. C., Lee, D. U., Noh, J. H., Kim, E. K. & Seok, S. I. Highly improved Sb<sub>2</sub>S<sub>3</sub> sensitized-inorganic-organic heterojunction solar cells and quantification of

- traps by deep-level transient spectroscopy. *Adv. Funct. Mater.* **24**, 3587–3592 (2014).
11. Zhang, S., Wei, S.-H., Zunger, A. & Katayama-Yoshida, H. Defect physics of the CuInSe<sub>2</sub> chalcopyrite semiconductor. *Phys. Rev. B* **57**, 9642–9656 (1998).
  12. Leite, M. S. *et al.* Nanoscale imaging of photocurrent and efficiency in CdTe solar cells. *ACS Nano* **8**, 11883–11890 (2014).
  13. Yin, W. J., Shi, T. & Yan, Y. Unique properties of halide perovskites as possible origins of the superior solar cell performance. *Adv. Mater.* **26**, 4653–4658 (2014).
  14. Tang, J. *et al.* Colloidal-quantum-dot photovoltaics using atomic-ligand passivation. *Nature Mater.* **10**, 765–771 (2011).
  15. Schmidt, J. *et al.* Surface passivation of high-efficiency silicon solar cells by atomic-layer-deposited Al<sub>2</sub>O<sub>3</sub>. *Prog. Photovolt.* **16**, 461–466 (2008).
  16. Choi, Y. C. *et al.* Sb<sub>2</sub>Se<sub>3</sub> sensitized inorganic–organic heterojunction solar cells fabricated using a single-source precursor. *Angew. Chem. Int. Ed.* **53**, 1329–1333 (2014).
  17. Zhou, Y. *et al.* Solution-processed antimony selenide heterojunction solar cells. *Adv. Energy Mater.* **4**, 201301846 (2014).
  18. Patrick, C. E. & Giustino, F. Structural and electronic properties of semiconductor-sensitized solar-cell interfaces. *Adv. Funct. Mater.* **21**, 4663–4667 (2011).
  19. Luo, M. *et al.* Thermal evaporation and characterization of superstrate CdS/Sb<sub>2</sub>Se<sub>3</sub> solar cells. *Appl. Phys. Lett.* **104**, 173904 (2014).
  20. Liu, X. *et al.* Thermal evaporation and characterization of Sb<sub>2</sub>Se<sub>3</sub> thin film for substrate Sb<sub>2</sub>Se<sub>3</sub>/CdS solar cells. *ACS Appl. Mater. Inter.* **6**, 10687–10695 (2014).
  21. Major, J., Treharne, R., Phillips, L. & Durose, K. A low-cost non-toxic post-growth activation step for CdTe solar cells. *Nature* **511**, 334–337 (2014).
  22. Mashtalir, O. *et al.* Intercalation and delamination of layered carbides and carbonitrides. *Nature Commun.* **4**, 1716 (2013).
  23. Hetzer, M. *et al.* Direct observation of copper depletion and potential changes at copper indium gallium diselenide grain boundaries. *Appl. Phys. Lett.* **86**, 162105 (2005).
  24. Jiang, C.-S. *et al.* Local built-in potential on grain boundary of Cu(In,Ga)Se<sub>2</sub> thin films. *Appl. Phys. Lett.* **84**, 3477–3479 (2004).
  25. Li, J. B., Chawla, V. & Clemens, B. M. Investigating the role of grain boundaries in CZTS and CZTSSe thin film solar cells with scanning probe microscopy. *Adv. Mater.* **24**, 720–723 (2012).
  26. Li, C. *et al.* Grain-boundary-enhanced carrier collection in CdTe solar cells. *Phys. Rev. Lett.* **112**, 156103 (2014).
  27. Sinsermsuksakul, P. *et al.* Overcoming efficiency limitations of SnS-based solar cells. *Adv. Energy Mater.* **4**, 201400496 (2014).
  28. Limpinsel, M. *et al.* An inversion layer at the surface of n-type iron pyrite. *Energy. Environ. Sci.* **7**, 1974–1989 (2014).
  29. Leng, M. *et al.* Selenization of Sb<sub>2</sub>Se<sub>3</sub> absorber layer: an efficient step to improve device performance of CdS/Sb<sub>2</sub>Se<sub>3</sub> solar cells. *Appl. Phys. Lett.* **105**, 083905 (2014).

## Acknowledgements

This work is supported by the Director Fund of WNLO, the National 1000 Young Talents project, the National Natural Science Foundation of China (NSFC 61274055, 91233121, 91433105, 21403078) and the 973 Program of China (2011CBA00703). The authors thank the Analytical and Testing Center of HUST, the Center for Nanoscale Characterization and Devices of WNLO and the Suzhou Institute of Nano-Tech and Nano-Bionics for the characterization support. Y. Yan at the University of Toledo and H. Zhong at the Beijing Institute of Technology are acknowledged for helpful discussions.

## Author contributions

Y.Z. and J.T. conceived the idea, designed the experiments and analysed the data. Y.Z. and L.W. carried out most of the characterizations and device optimizations. S.C. performed the theoretical simulations and analysed the results. S.Q. and X.L. initialized the RTE process. J.C., D.-J.X., M.L. and Y.C. participated in the device optimization and data analysis. Y.Ch. helped with the manuscript preparation. E.H.S. and J.T. wrote the paper; all the authors commented on the manuscript.

## Additional information

Supplementary information is available in the [online version](#) of the paper. Reprints and permissions information is available online at [www.nature.com/reprints](http://www.nature.com/reprints). Correspondence and requests for materials should be addressed to J.T.

## Competing financial interests

The authors declare no competing financial interests.



## Methods

**Solar cell fabrication.** All devices were deposited on glass-coated  $\text{SnO}_2\text{:F}$  supplied by Kaivo (Zhuhai, China) that had been cleaned using a detergent, acetone, isopropanol and water rinse in sequence. Chemical bath deposition ( $\text{CdSO}_4$ , 65 °C, 16 minutes) was used to deposit a CdS layer of about 60 nm thickness. A  $\text{CdCl}_2$  post-treatment was applied to the CdS buffer layer: (1) a  $\text{CdCl}_2$  (99%, Aladdin) anhydrous methanol saturated solution (about 20 mg ml<sup>-1</sup>) was spin coated onto the CdS layer and then rinsed with methanol; (2) the treated CdS layer was baked on a hot plate at 400 °C for five minutes in air. An  $\text{Sb}_2\text{Se}_3$  layer was deposited by RTE in a tube furnace (MTI, Hefei, China). The set-up is shown schematically in Supplementary Fig. 1.  $\text{Sb}_2\text{Se}_3$  powder was placed on the AlN plate inside the quartz boat, and the FTO/CdS substrate was placed on top of the quartz boat (0.8 cm distance from the  $\text{Sb}_2\text{Se}_3$  powder) with the CdS side facing down. When the pressure was reduced to below 10 mtorr, the film deposition was initiated. The deposition process was to preheat the source and substrate at 300 °C for 15 minutes, then ramp the temperature up to approximately 550 °C within 30 seconds, maintain this temperature for 30 seconds and then turn off the heating and allow the film to cool naturally to ~150 °C. Films were then taken out for Au deposition. Gold back contacts (0.095 cm<sup>2</sup>) were thermally evaporated using the electron beam and a resistance evaporation thin-film deposition system (Beijing Technol Science Co. Ltd) under a vacuum pressure of  $5 \times 10^{-3}$  Pa.

**Solar-cell performance measurement.** The devices were measured under a simulated 100 mW cm<sup>-2</sup> AM1.5G irradiation, which was generated through a 3A solar simulator with a Xe light source (450 W, Oriel, Model 9119). A Keithley 2400 was applied to measure the current–voltage characteristics in air. The device area (0.095 cm<sup>2</sup>) was defined by the size of the gold electrodes. For the in-house measurements, no temperature control was applied. The scan rate was 0.1 V s<sup>-1</sup>, and no hysteresis was observed between the forwards ( $J_{\text{SC}}$  to  $V_{\text{OC}}$ ) and reverse ( $V_{\text{OC}}$  to  $J_{\text{SC}}$ ) scan (Supplementary Fig. 7). We also applied aperture (using a metal mask to define the incident light) and mechanical scribing to measure some of the devices and obtained comparable device efficiencies (Supplementary Figs 8 and 9). The device was further independently certified by the Newport Cooperation (American Certificate Number 1017 issued on 16 May 2014, without aperture). The ageing of the devices below 85 °C with 85% humidity was applied in a desktop constant-temperature and humidity testing machine, QA-HPZ-30 (Dongguan Cheng Yang Instruments Industry Co. Ltd).

**XRD.** XRD measurements were performed using a Philips diffractometer (Xpert PRO MRD) with a step of 0.017 ° and a step time of 10.16 seconds. The lines used were Cu  $K_{\alpha 1}$  and Cu  $K_{\alpha 2}$  with wavelengths of 1.54060 nm and 1.54443 nm, respectively.

**TEM and selected area electron (SAED) characterization.** Samples for TEM and SAED analyses were prepared by ablating the certified device using a FEI Quanta 3D FEG-FIB. A thin Pt layer was first deposited on top of the device for protection. TEM images and SAED measurements were taken using a FEI Titan G2 60–300 Probe Cs Corrector STEM operating at 300 kV.

**KPFM.** KPFM was performed on a grounded  $\text{Sb}_2\text{Se}_3$  sample using a NT-MDT Dimension 3100 system. The topography and surface potential were simultaneously measured using a Pt-coated silicon probe (NT-MDT, HQ: NSG11/Pt,  $f_0 \approx 150$  kHz,  $k \approx 5.5$  N m<sup>-1</sup> and sampling rate 0.25 Hz). The surface potential was calculated from the electrostatic force between the probe tip and the surface of the sample using a lock-in amplifier. The scanning area was 2.5  $\mu\text{m} \times 2.5 \mu\text{m}$  of 512  $\times$  512 pixels. The minimal distance between two scanned points was about 5 nm, and the potential measurement limit and resolution were 10 mV and 1 mV, respectively.

**EBIC measurement.** The device was cleaved by hand after scribing on the back and loaded into an SEM vacuum chamber for EBIC measurements. SEM images were taken on a Quanta 400 FEG FEI microscope equipped with a SmartEBIC (Gatan, Inc.). The gold back contact was contacted to the preamplifier by a small micromanipulator to enable current measurements. The electron-beam voltage was 20 kV and the working distance was about 10.5 mm. Images were processed using the Digital micrograph software.

**Simulation methods.** The structural relaxation and electronic structure of  $\text{Sb}_2\text{Se}_3$  were calculated within the density functional formalism as implemented in the VASP code<sup>30</sup>. For the exchange–correlation potential, we used the non-local vdW-DF (van der Waals density functional) method proposed by Dion *et al.*<sup>31</sup> to describe the van der Waals interaction. The interaction between the core electrons and the valence electrons is included in the frozen-core projector augmented-wave pseudopotentials. An energy cut-off of 400 eV was applied in all cases. For Brillouin-zone integration, we used the  $4 \times 4 \times 12$  Monkhorst-Pack  $k$ -point mesh for the 20-atom primitive cell, and  $2 \times 6 \times 1$  ( $2 \times 2 \times 1$ ) meshes for the (100) [(010)] surface slab models. The lattice vectors of the primitive cell and the atomic positions were fully relaxed by minimizing the quantum mechanical stresses and forces.

## References

30. Kresse, G. & Furthmüller, J. Efficient iterative schemes for *ab initio* total-energy calculations using a plane-wave basis set. *Phys. Rev. B* **54**, 11169–11186 (1996).
31. Dion, M., Rydberg, H., Schröder, E., Langreth, D. C. & Lundqvist, B. I. *Phys. Rev. Lett.* **92**, 246401 (2004).